

Failure Detection in an Annular Combustion Chamber with Experimental and Numerical Methods

Hennecke C, Von der Haar H* and Dinkelacker F

Institute of Technical Combustion (ITV), Leibniz University Hanover, Welfengarten 1A, 30167 Hanover, Germany

Abstract

The inspection of aircraft engines is a complex and time-consuming process, usually requiring the disassembly of the engine or extensive baroscopic examinations. Thus, a method is to be developed in order to evaluate the state of the jet engine prior disassembling by analysing the state and structure of the exhaust jet. This could be done for instance with an analysis of the density, temperature, velocity or concentration distribution in a cross section through the exhaust jet. Assumptions are that failures inside the engine influence the exhaust jet in a measurable way and by means of numerical simulations it is possible to evaluate the flow and combustion process beginning in the engines' interior through the exhaust gas jet. A generic study on a pilot scale annular combustion chamber is the basis to show the feasibility of this approach. The combustion chamber consists of eight premixed swirl burners. One of the burners has the option to be operated independently from the others on defined varied operation points. This simulates a failure state of a burner which allows an investigation of the correlation between defined failure states and resulting pattern in the exhaust jet. Detailed techniques are applied to evaluate the approach and the detection limits. Firstly, extensive numerical simulations of possible failure states were conducted to compare with measurements. Secondly, the particle image velocimetry (PIV) technique was used to measure the velocity field in the measurement plane downstream of the combustion chamber. Local reductions of the thermal power lower the acceleration of the exhaust gas and influence the velocity field. Thirdly, species concentrations were measured with a movable probe, evaluated by Fourier-transform infrared (FTIR) spectroscopy. Species concentration information can indicate combustor failures like locally mistuned air-fuel-ratio, serious defects on the swirl vanes, or oil leakages.

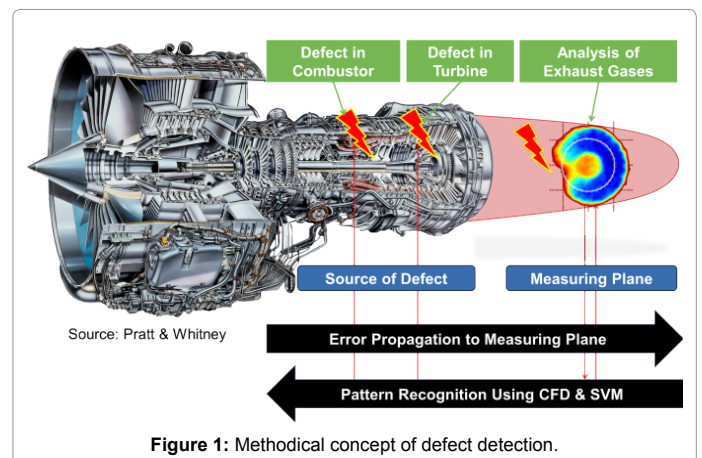
Keywords: Combustion chamber defect detection; Aircraft engines; Turbulent combustion; Particle Image Velocimetry (PIV); Fourier-Transform Infrared Spectroscopy (FTIR); Numerical simulation

Introduction and Methodical Approach

Defects in combustion chambers of aircraft engines might reduce the performance and represent a security risk. A methodology is sought to enable a diagnosis during operation of the aircraft engine on the wing. This would allow decisions on the timing and extent of regeneration measures at an early stage. Thus, operation cycles may be lengthened or shortened depending on demand. Furthermore, the necessary regeneration process could be planned and prepared in detail before the disassembly of the engine, leading to a faster and more efficient repair procedure.

The approach is based on the assumption that defects in the combustion chamber have a significant influence on the internal flow, which induce detectable pattern in the exhaust jet (Figure 1). The distribution of velocity, density, and temperature or gas composition provides information about the status of the combustion and flow processes inside the combustion chamber and may be measured with spatial resolution by appropriate measurement techniques. Due to the high mechanical and thermal load behind an aircraft engine, optical measurement techniques are preferable for real application. A further assumption is that numerical simulation methods can describe the linking process between the failure source inside the combustion chamber and the measured texture of the exhaust jet. In that case, damages at the real engine can be detected with appropriate exhaust jet diagnostics without disassembling the engine. The feasibility of this approach has already been shown in first steps [1–4].

Since measurements on real aircraft engines are complex, experimental studies are carried out on an atmospheric annular combustion chamber in the laboratory. This allows for a detailed investigation whether combustor errors can be localized by analysing



patterns in the exhaust jet, as this combustion chamber is easily accessible for measurement techniques, and well defined operating points can be compared with numerical simulations.

Following this methodical concept, it is the aim of this work

*Corresponding author: Von der Haar H, Institute of Technical Combustion (ITV), Leibniz University Hanover, Welfengarten 1A, 30167 Hanover, Germany, Tel: +49 511 762 - 19835; E-mail: vonderhaar@itv.uni-hannover.de

Received May 18, 2017; Accepted June 12, 2017; Published June 15, 2017

Citation: Hennecke C, Von der Haar H, Dinkelacker F (2017) Failure Detection in an Annular Combustion Chamber with Experimental and Numerical Methods. J Aeronaut Aerospace Eng 6: 193. doi: 10.4172/2168-9792.1000193

Copyright: © 2017 Hennecke C, et al. This is an open-access article distributed under the terms of the Creative Commons Attribution License, which permits unrestricted use, distribution, and reproduction in any medium, provided the original author and source are credited.

to prove, if influences of the faulty burner are detectable in a cross section in the exhaust gas jet, both with numerical simulation and with experimental methods. Particularly it is to examine which deviations can be measured and which are hidden from the mixing process between the failure location and the measurement plane, dependably. This gives an indication of the minimal observable failure which can be detected sufficiently. Moreover, it has to be studied if a certain measured quantity is appropriate to distinguish different types of failures or if more than one quantity is required to prevent confusion.

Model Combustion Chamber and Investigated Operation Points

For the verification of the approach, a simplified annular combustion chamber has been developed, as shown in Figure 2. The combustion chamber consists of an array of eight premixed-operated methane-air swirl-burners, which are arranged on a circle with a diameter of 210 mm. Every burner (right picture) is composed out of a tube with an inner diameter of 28 mm in which a swirl generator consisting of five blades and a turbulence grid are mounted. The combustion chamber (left picture) is outwardly and inwardly confined by cylindrical quartz glass rings for optical access. The outer diameter is 310 mm and the inner diameter is 105 mm, whereas the height is 200 mm. The inner glass ring is cooled by an air flow from the inside.

For the investigations of defects in a combustion chamber, the test-rig provides the option to operate the chamber with defined failures. One of the eight burners can be varied in its operating condition in the chamber independently from the other ones.

The current work focuses on two types of errors in aircraft engines. In study A, the thermal power of the variable burner is reduced while

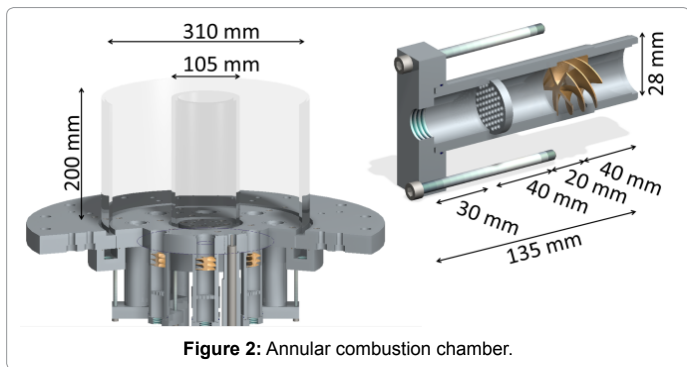


Figure 2: Annular combustion chamber.

Cases	P_{Array}	λ_{Array}	P_{Single}	λ_{Single}
Ref_15 kW	7×15 kW	1.0	15 kW	1.0
Fail_14 kW	7×15 kW	1.0	14 kW	1.0
Fail_13 kW	7×15 kW	1.0	13 kW	1.0
Fail_12 kW	7×15 kW	1.0	12 kW	1.0
Fail_11 kW	7×15 kW	1.0	11 kW	1.0
Fail_10 kW	7×15 kW	1.0	10 kW	1.0

Table 1: Investigated operating points for study A: Variable burner operates with reduced load.

Case	P_{Array}	λ_{Array}	P_{Single}	λ_{Single}
Ref_15 kW	7×15 kW	1.0	15 kW	1.0
Fail_λ 0.8	7×15 kW	1.0	15 kW	0.8
Fail_λ 1.2	7×15 kW	1.0	15 kW	1.2

Table 2: Investigated operating points for study B: Variable burner operates with changed air-fuel-ratio.

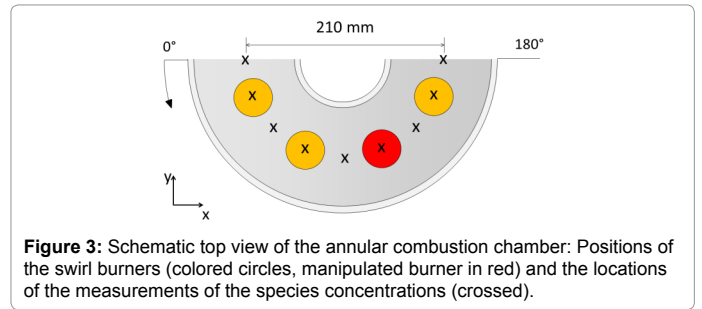


Figure 3: Schematic top view of the annular combustion chamber: Positions of the swirl burners (colored circles, manipulated burner in red) and the locations of the measurements of the species concentrations (crossed).

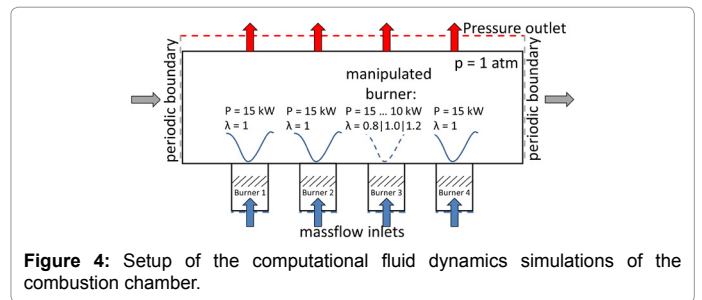


Figure 4: Setup of the computational fluid dynamics simulations of the combustion chamber.

holding the other burners constant on the thermal power of 15 kW. Here, all burners are operated with stoichiometric air-fuel-ratio $\lambda=1.0$. The power of one burner is reduced stepwise down to 10 kW (Table 1). With this study, it is investigated which of these rather small variations are still detectable.

In study B, one burner is varied in its air-fuel-ratio, either being reduced to $\lambda_{Single}=0.8$ (fuel-rich case) or being increased to $\lambda_{Single}=1.2$ (fuel-lean case) while the other seven burners are operated with $\lambda=1.0$. Here the thermal power is hold constant at 15 kW for each burner. Table 2 summarizes the operation conditions.

Figure 3 shows the top view of the combustion chamber. The position of the manipulated burner is marked in red. The following evaluations are done for this view: The crosses in the graphic illustrate the positions of the FTIR measurements, the angles are used in the line plots below in this paper.

Numerical Setup of the Computational Fluid Dynamics - Simulations

The connection between the sources of a failure inside the combustor and the flow field further downstream is numerically calculated with the method of the three-dimensional computational fluid dynamics (CFD) with additional models for the reaction processes. The Reynolds-averaged Navier-Stokes simulation (RANS) approach is used. For the calculation, the annular combustion chamber is resolved with a numerical mesh of approximately 18 million tetrahedral cells. Flow and turbulence are determined using the k- ω SST model [5]. The reaction process is modelled with a partially premixed combustion model, consisting of the extended coherent flame model for the premixed regime [6] combined with the presumed probability density function (pre-PDF) as a mixture fraction approach [7–9].

The geometry of the annular combustion chamber is represented by a 180° segment. Periodic boundary conditions ensure accurate transitions on the cut planes, to save computational cost (Figure 4). The third burner can be manipulated individually to represent the failing burner.

For the reference case, each burner is fuelled by a premixed inlet mass flow of 5,471 g/s at a temperature of 300 K, equivalent to a

thermal power of 15 kW of methane-air-mixture at stoichiometry and atmospheric conditions. The pressure outlet is set to 101330 hPa.

Experimental Setup of the Particle Image Velocimetry

The flow on the model combustors' exit is analysed using the particle image velocimetry (PIV) method with a stereoscopic approach [7,9]. One aspect is to prove, if the manipulated burner has a detectable impact on the exhaust jet. A second aspect is to verify the hypothesis that a correlation between the failure source inside the combustor and the measurable failure pattern on the exit plane is given by applying the computational fluid dynamics (CFD) technique. The comparison

between measurement and simulation is of importance to see, if the method of CFD simulation would be applicable also in complex aircraft engine geometries, to locate failures inside the engine, that are identified through the measured pattern in the exhaust gas jet.

PIV is a minimally invasive flow measurement technique that allows a two- or three-dimensional flow field to be acquired by tracking the movement of small particles that are added to the fluid. Within a light-sheet plane illuminated by a pulsed laser the particles are imaged in consecutive pictures with defined time-interval. With the cross-correlation method the velocity field can be determined [10,11].

Due to the highly three-dimensional flow field of the swirl burners flow, a stereoscopic PIV setup was applied (Figure 5).

The measurement plane is aligned horizontally. As light source the Litron Nano L 135-15 PIV double pulse laser with a wavelength of 532 nm and a pulse energy of maximum 135 mJ per cavity was used. A light sheet is formed with a suitable light sheet optic consisting of three lenses. The distance between the measurement plane and the optics is 1000 mm. As tracer, inert TiO_2 particles are mixed to the flow, following the flow through the flame. For the PIV measurements two 14-bit CCD cameras with a resolution of 1600×1200 pixels (pixel size: $7.4 \mu\text{m} \times 7.4 \mu\text{m}$, sensor size: $11.8 \times 8.9 \text{mm}^2$), equipped with 50 mm lenses with a fixed focal length of $f / 1.4$ are used with laser line filters for $532 \text{nm} \pm 3 \text{nm}$. The lens and the camera are connected via manual tilt adapters according to the Scheimpflug criterion [12,13], whereby the camera axes are inclined by the angle $\theta=50^\circ$ against the normal of the measuring plane. The cameras are located approximately 830 mm above the measuring plane. The time interval between the pictures was $60 \mu\text{s}$ for the 200-mm evaluation plane and $20 \mu\text{s}$ for the 20-mm plane cutting the flame zone.

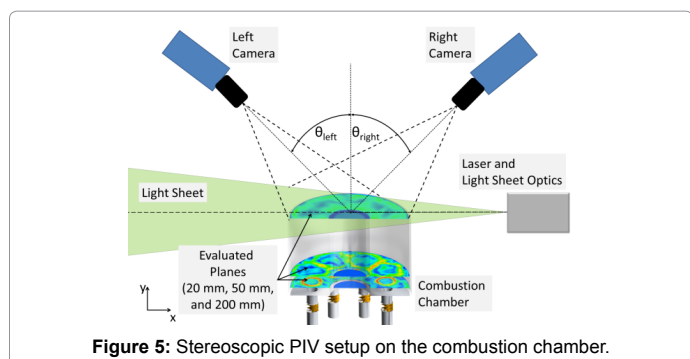


Figure 5: Stereoscopic PIV setup on the combustion chamber.

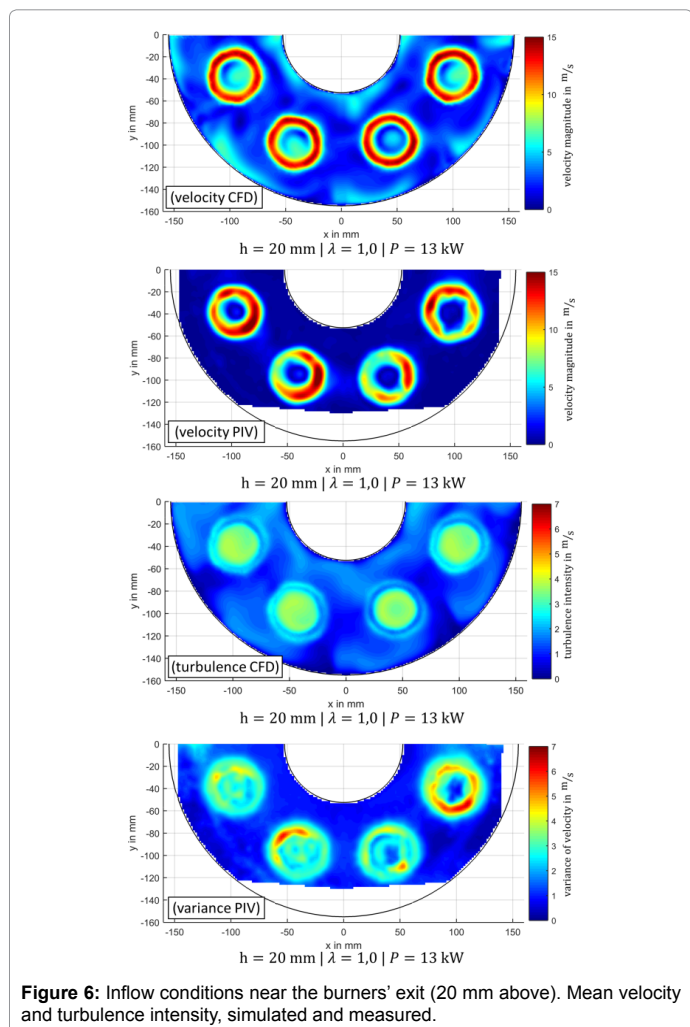


Figure 6: Inflow conditions near the burners' exit (20 mm above). Mean velocity and turbulence intensity, simulated and measured.

Verification of Simulated and Measured Inlet Flow Conditions

The simulation domain of the flow and combustion process starts inside the burner 40 mm prior the turbulence grid. The calculated and measured flow conditions are compared near the burners' exit which practically was possible at the height of 20 mm above the burner plane (Figure 5). For the following results, generally a half-section of the combustion chamber is shown in the measurements and the simulation (Figure 6). The single variable burner is the lower right one (Figure 3). For the comparison, all eight burners are operated in similar way, here exemplary the case Fail_13kW is shown. Figure 6 shows the spatial distribution of the velocity magnitude in the 20-mm plane from simulation (first image) and from measurement (second image). The structure of the flow field is sufficiently similar, although the local velocity distributions in the measured cases vary to some extent close to the burner exit. Also, the calculated (third image) and measured turbulence intensity (fourth image) is sufficiently comparable, showing the turbulence intensity fluctuation to be in the range of 4 to 5 m/s.

Failure Detection for Study A by Evaluation of the Velocity Field

The spatial distribution of the velocity magnitude is shown in Figure 7 for the simulation and in Figure 8 for the PIV measurement at the exit plane of the combustion chamber, located 200 mm downstream of the burner plane.

In study A the faulty burner is operated with varied thermal power. In the top case the variable burner is operating identically to the other

burners (reference case). The calculated three-dimensional flow field shows a periodic flow pattern with velocity magnitudes in the range of 3 to 4 m/s in the middle section of the ring, with 5 to 6 m/s near the inner ring and with periodic flow pattern near the outer ring.

The measured flow field shows a rather similar velocity distribution concerning the flow pattern. The velocity magnitudes vary more than in the calculation, with a range of 2 to 3 m/s in the middle section and 5 to 6 m/s near the inner and the outer ring.

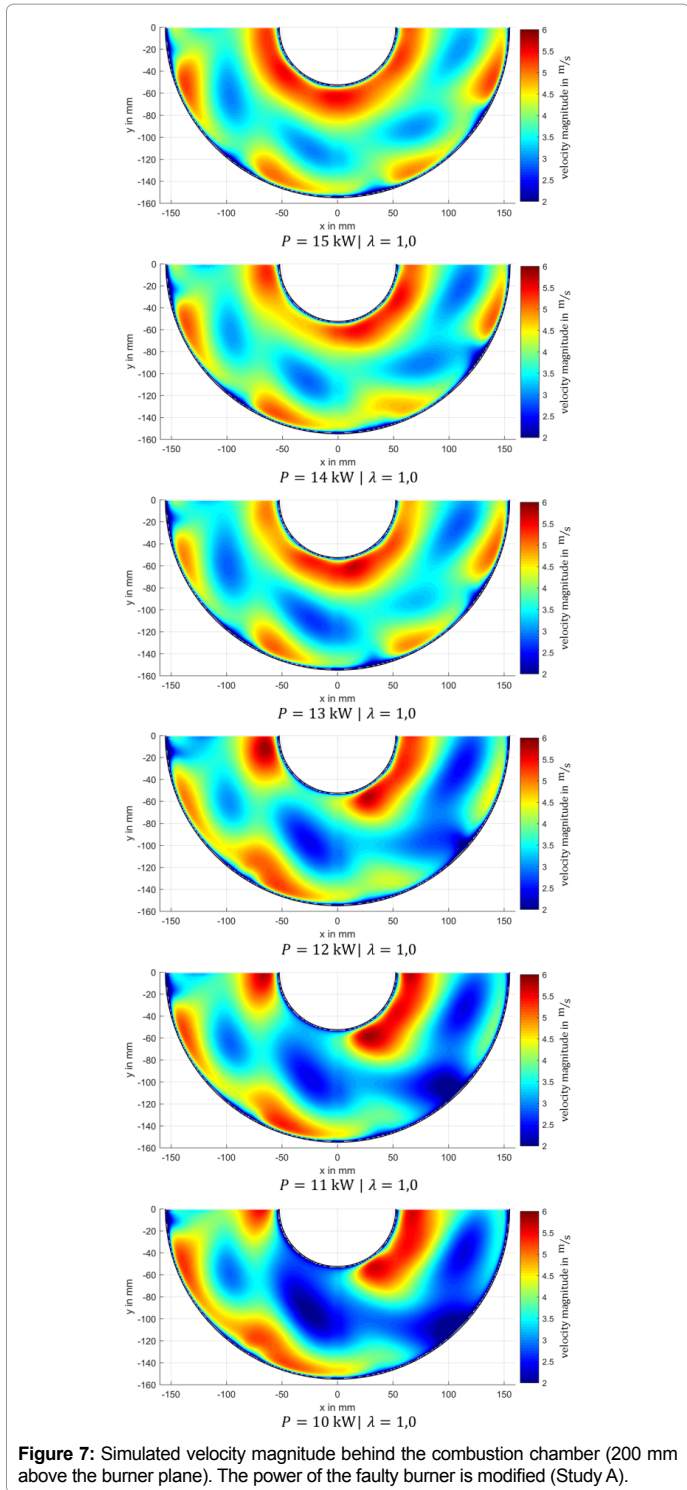


Figure 7: Simulated velocity magnitude behind the combustion chamber (200 mm above the burner plane). The power of the faulty burner is modified (Study A).

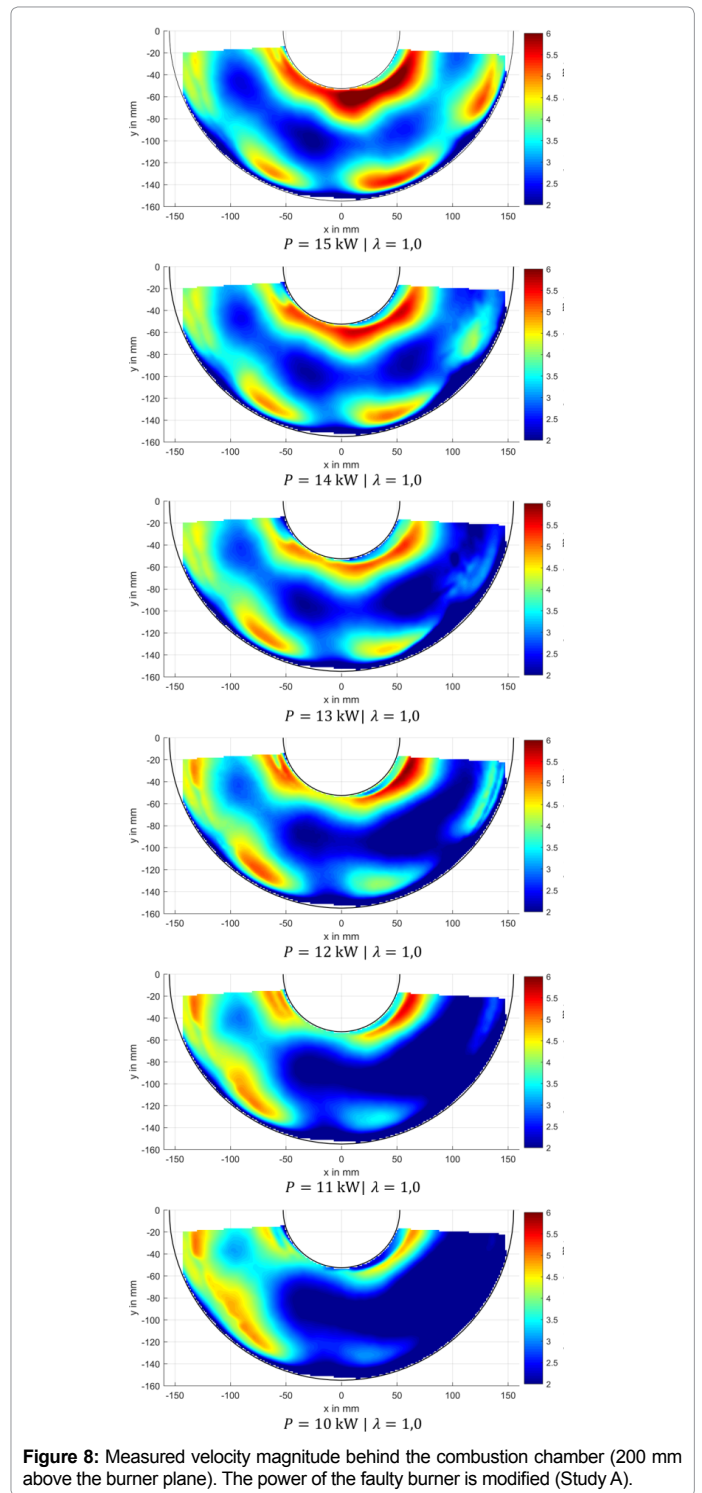


Figure 8: Measured velocity magnitude behind the combustion chamber (200 mm above the burner plane). The power of the faulty burner is modified (Study A).

A significant deviation of the velocity field is detectable, if the faulty burner is operating with 13 kW thermal power instead of the 15-kW reference power (third row). For the 12 kW and lower cases the deviation is clearly visible in the outer part of the velocity field - both for the simulation and the experimental results. The influence of the deviating burner extends the range of the initial 45° segment on the burner plane and the whole flow field is affected increasingly with growing deviation of the faulty burner.

In Figure 9 circumferential profiles (being determined along the middle ring with a width of 7.5 mm, averaged over 1000 single measurements) of the measured velocity magnitude at the exit of the combustion chamber show that the influence of the faulty burner is clearly visible when its power is reduced. It should be noted that the variable burner is positioned at 112.5°, while the observed velocity minimum is moved by about 20° to the 135° position. This is understandable from the highly three-dimensional interacting flow field of the different swirl burners (swirl direction is counter-clockwise) which leads to some movement of the velocity minima behind each burner in circumferential direction.

From the measurement of the velocity magnitude at the exit plane of the combustion chamber it can be concluded that the velocity field is still dominated from the swirling flow of the individual burners. Their flow field is strongly interacting, but the influence of the modified burner can be detected clearly. From the comparison with the numerical simulation it can be concluded that the numerical simulation is able to represent the essential features of the flame and flow pattern in the combustion chamber.

In study B the faulty burner is modified concerning its air-fuel-ratio while the other burners operate in the reference state and the thermal power of the variable burner is hold constant. Figure 10 shows the simulated velocity magnitude distribution at the exit plane of the combustion chamber. The reference case is shown in the middle. If the faulty burner is operated in the lean mode ($\lambda=1.2$, top image) the velocity distribution increases above this burner. This results from the increased flow rate at constant power. If the faulty burner is operated rich ($\lambda=0.8$, bottom) the air-fuel-rate is reduced and less fuel is consumed. Both effects are leading to lower velocities in the burnt part, as is clearly visible.

Variation of the local air-fuel-ratio leads to significantly modified chemical processes in the flame which results in different composition in the exhaust jet cross section.

Before getting into the experimental and numerical details of this issue, one other aspect is discussed with respect to the future aim of defect classification out of measured exhaust profiles.

The future aim is the subsequent implementation of an automatic defect classification out of the exhaust profile measurement. For the classification of the corresponding defect, a unique pattern is necessary, which is specific for one case of failure, as otherwise a faulty defect assignment could occur. Figure 11 demonstrates the influence of two different defects on the simulated velocity field at the exit plane of the model combustion chamber. The upper image shows the velocity

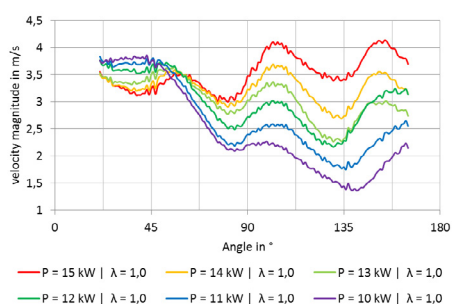


Figure 9: Influence of reduced power of the variable burner positioned at 112.5°, measured radial velocity magnitude (on diameter 205 mm) at the combustor exit plane.

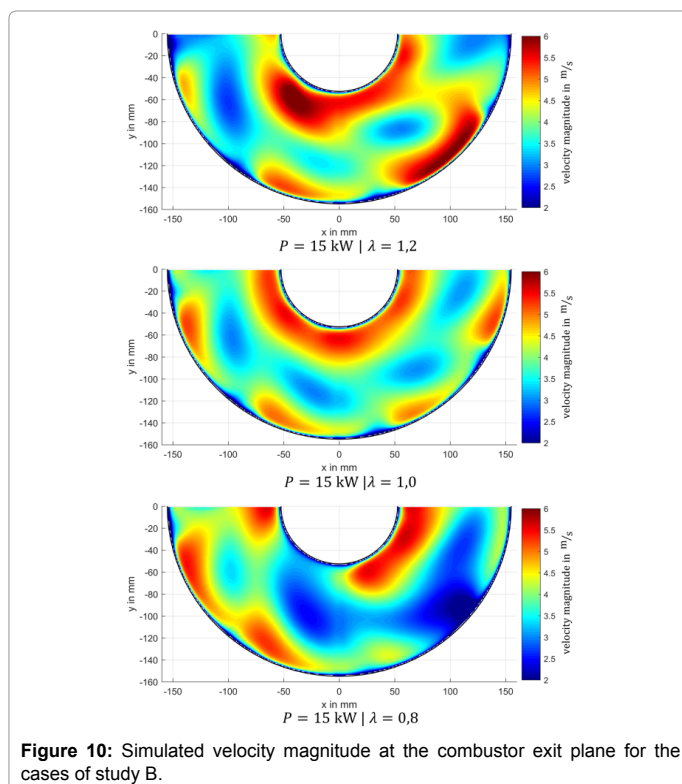


Figure 10: Simulated velocity magnitude at the combustor exit plane for the cases of study B.

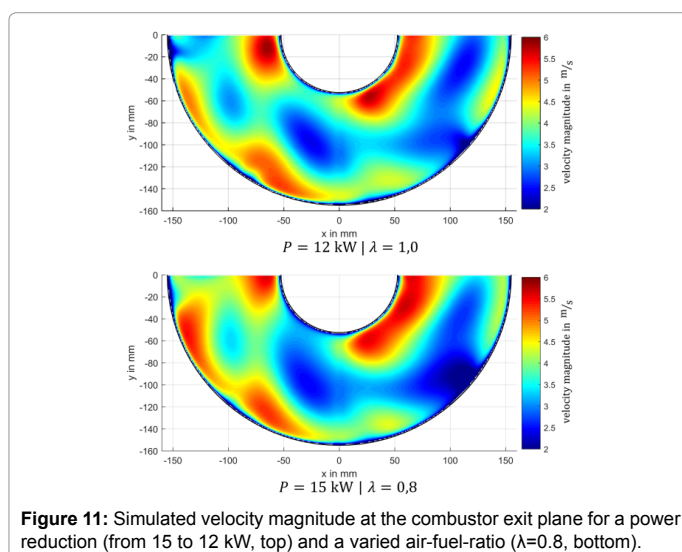


Figure 11: Simulated velocity magnitude at the combustor exit plane for a power reduction (from 15 to 12 kW, top) and a varied air-fuel-ratio ($\lambda=0.8$, bottom).

distribution for a power reduction of 20% to 12 kW of the faulty burner. The second graphic shows the influence of a varied air-fuel-ratio of 20% to $\lambda=0.8$ at initial thermal power of 15 kW. Both defects lead to a quite similar velocity distribution, so that an automatic defect classification will probably not be successful.

This example demonstrates that the use of only one measured quantity is not sufficient for a robust defect classification. Therefore, further quantities have to be taken into account.

Determination of Species Concentration Distributions

In Figure 12, the calculated CO concentration is shown for these two defect cases. The CO concentration depends strongly on the

stoichiometric condition in the flame and large amounts of CO due to the incomplete combustion in the fuel-rich case. With this additional information, a differentiation between the two different defects shown in Figure 11 is possible. Figure 12 shows also the spatial distribution of the exhaust flow deriving from the manipulated burner.

In Figure 13, the CO₂ concentration is shown for all three cases of the study B. Also, this quantity can give clear additional information to the velocity magnitude, indicating the influence of the burner failure with respect to varied stoichiometric ratio. The spatial distribution of the exhaust gas coming from the varied single burner is clearly visible.

In the experimental study, additionally species concentration measurements are done at the exit plane of the combustion chamber.

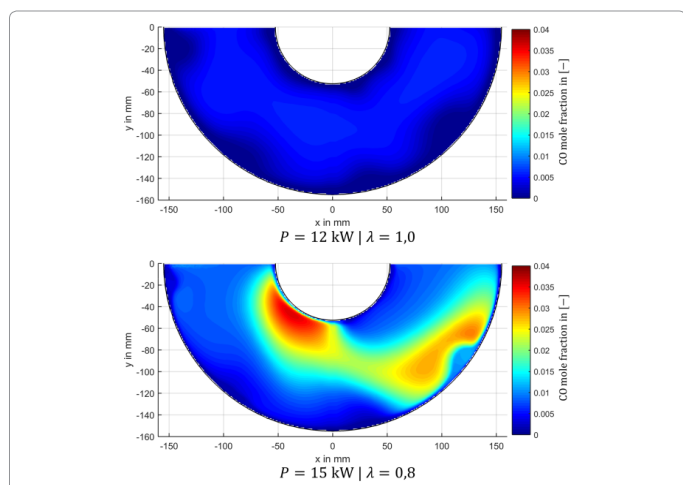


Figure 12: Simulated CO mole fraction at the combustor exit plane for a power reduction (from 15 to 12 kW, top) and a varied air-fuel-ratio ($\lambda=0.8$, bottom).

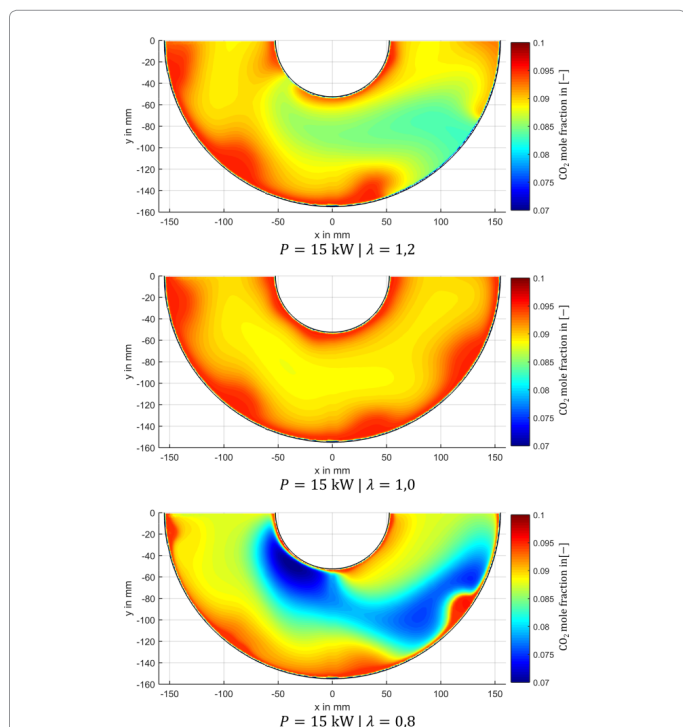


Figure 13: Simulated CO₂ mole fraction at the combustor exit plane for the cases of study B.

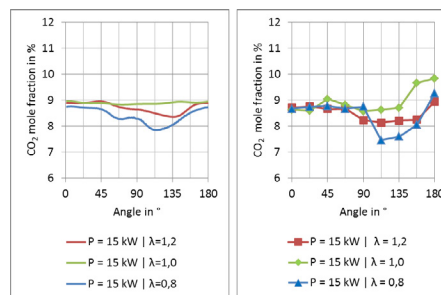


Figure 14: Circumferential profile of calculated (left) and measured CO₂ mole fraction (right) at the combustor exit plane for the cases of study B.

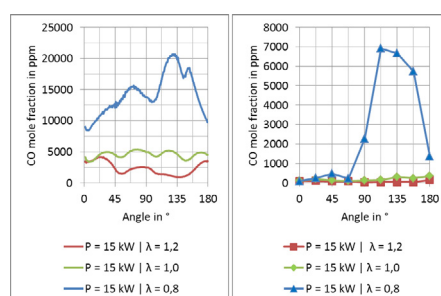


Figure 15: Circumferential profile of calculated (left) and measured CO mole fraction (right) at the combustor exit plane for the cases of study B.

For this purpose, a fourier-transform infrared (FTIR) spectrometer has been used. The FTIR measurement system allows the determination of the concentration of the gas components CO, CO₂, H₂O, NO, NO₂ simultaneously by extracting samples of the exhaust gases. The samples are extracted in the measurement half plane at nine specific positions by a moveable and heat resistant exhaust probe, as shown in Figure 3. The measurement points are arranged in a semi-circle of 210 mm diameter. The recording rate of the used FTIR system is 1 1/s. The measurement period for every position is 45 s and the averaged results are shown in the following. Exemplary measured concentration profiles are discussed in the following for varied air-fuel-ratio of study B.

Figure 14 the measured CO₂ concentrations on the nine measurement points as well as the calculated CO₂ concentration along the circumferential middle line is shown. In the reference case, all burners are operated at air-fuel-ratio $\lambda = 1.0$ (green). In the failure cases the faulty burner is operated either in the lean mode ($\lambda=1.2$, red) or in the rich mode ($\lambda=0.8$, blue). For the reference case the simulation shows a constant CO₂ concentration of 8.8%, while the measurements show the same CO₂ concentration in most of the measurement points, while for the two right positions the CO₂ concentration increased to 8.7% and 9.7%. The reason for this unexpected inhomogeneity is not clear. For the fuel, lean condition at $\lambda=1.2$ both the simulation and the FTIR measurements show a reduction of the CO₂ concentration. Between 90° and 157° similar concentration profiles can be found, where the CO₂ concentration is in the same order: 8.4% (simulation) and 8.2% (experiment). The results confirm that the failure can be detected with both methods clearly.

Also, the dispersion of the failure pattern can be analysed. Assuming the initial width of the failure region to be 45° (one out of eight burners), the detected width of the failure region reaches about 75° for the measurement and 60° for the simulation (defined as full width at half maximum, FWHM, of the spatial variation in the concentration

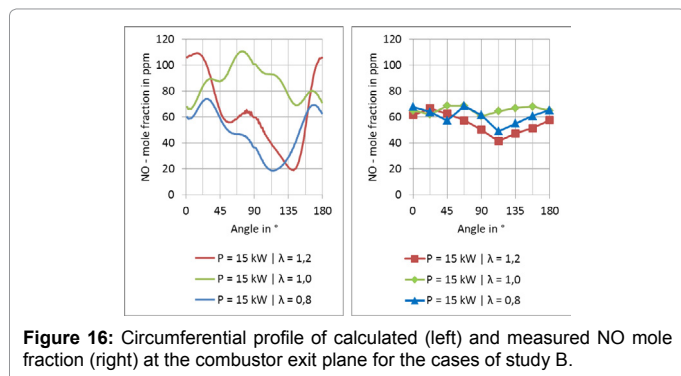


Figure 16: Circumferential profile of calculated (left) and measured NO mole fraction (right) at the combustor exit plane for the cases of study B.

profile) at the measurement distance of 200 mm above the burner plane. This increase of the failure width in the exhaust path is reasonable, and the rather similar increase of this width between simulation and experiment confirms that the simulation method is applicable for the numerical prediction of the correlation between failure source and detection plane.

For the fuel-rich condition at $\lambda=0.8$ both the experiment and the simulation profiles of the CO_2 concentration deviation are clearly visible with a full width of 60° for the measurement and of 75° for the simulation, where the simulation shows a broader dispersion region with low deviation.

In Figure 15 the CO concentration profiles are compared. Here the comparability between measurement and simulation is lower than for the CO_2 concentration. The simulations show significantly increased CO levels compared to the measurement also for the stoichiometric and the fuel lean case, while the measured values are near zero here, as can be expected for nearly complete combustion in these cases. For the fuel, rich condition both simulation and experiment show a strongly increased CO level, as expected for this partially reacting case. The calculations show considerable higher absolute values, which are not reasonable. Here, the reaction model for this intermediate species is definitely not realistic.

However, the relative CO levels are well predicted for the simulation in correspondence with the measured values, if the significant increase for the fuel rich burning faulty burner is regarded. If the CO profile is compared here, the simulation predicts an increased dispersion of the CO molecules over a broader circumferential range. The FWHM values of the spatial distribution are approximately 90° for the simulation and 70° for the experiment.

As a third example the calculated and measured NO concentration profiles are shown in Figure 16. The simulations show the same NO levels as measured, but a stronger reduction for the lean and the rich case. For the homogeneous reference case the measured NO concentration is constantly approximately around 65 ppm. Under lean and rich conditions the measured NO concentration decreases above the position of the manipulated burner. This trend follows the expectation of thermal NO_x formation, as the flame temperature is reduced in both cases and as thermal NO_x depends strongly on flame temperature. The local reduction from 65 ppm to 50 ppm (fuel-rich) or 43 ppm (fuel-lean) is significantly detectable. The FWHM values of the reduced NO zones are between 45° and 60° . This region is narrower than has been detected for the other concentrations. This effect might originate from the non-linear thermal NO formation process as a function of local temperature, which leads to the smaller gap. The reference case of the calculated NO concentration profiles shows a

quite inhomogeneous behaviour. However, the calculated mean values are reasonable: 85 ppm for the $\lambda=1.0$ reference case (measurement: 65 ppm). The strong reduction for both the lean and the rich case at 112.5° is qualitatively in good agreement. The calculated FWHM values are between 70° and 80° .

Not shown here are measured and calculated profiles of NO_2 and H_2O . Also, here the influence of the modified burner is detectable both from the numerical simulation and from the FTIR measurement.

The analysis of the circumferential species concentration profiles for the examples of the faulty burner shows, that the failure has a detectable influence on the concentration profile at the exit of the combustion chamber. The width of the influenced area at the exit is relatively broadened 60° up to 90° in comparison to an initial burner segment of 45° . This can be explained by turbulent mixing leading to a broadened mixing zone.

For these cases both simulation as well as species measurements may be applicable since the trends for both the fuel-rich as well as the fuel-lean cases are distinguishable. The reaction model predicts the CO_2 concentration in good accordance to the species measurements, but is not fully suited for the quantitative CO and NO concentration calculation.

Discussion and Conclusion

Detailed studies were done on an annular combustion chamber where the operation condition of one swirl burner can be varied in a defined way with respect to the other seven swirl burners. The two studies discussed in this work show that defined failures can be detected in a measurement plane behind the combustion chamber. In study A the thermal power of the variable burner in the annular combustion chamber was reduced from the references state (15 kW) in 1 kW steps down to 10 kW, representing a deficient fuel supply. For the investigated cases deviations in the range of 1 kW are already leading to a distinguishable modified pattern at the exhaust plane of the combustion chamber. For deviations above 2 kW (10% to 15% deviations) the failure pattern is clearly detectable for the different measurement techniques as well as from the simulation.

Only considering one quantity like the velocity field might be misleading for a classification of defects. An example has been presented, showing a similar velocity pattern originating from rather different failure types.

Therefore, the consideration of species concentrations is proposed as a useful additive. In study B the faulty burner was operated either in a fuel-lean mode ($\lambda=1.2$) or a fuel-rich mode ($\lambda=0.8$) while the other seven burners were operated stoichiometrically. The resulting deviation in the simulated flow field and the concentration profiles e. g. CO_2 , CO or NO at the exhaust plane are detectable for these failures as well.

The width of the resulting streak in the velocity field or species concentrations increases in size while proceeding downstream due to turbulent mixing.

The studies done on this annular combustion chamber are simplified to the situation in a real jet engine combustion chamber. For the application in real jet engines it is of interest if the methodology can be applied there. For the approximation of the potential it can be emphasised that the residence time in the real jet engines' combustion chamber is even lower than in this simplified model combustion chamber. The lateral turbulent mixing between the jet engine flames can be expected to be lower than in the investigated annular combustion

chamber. Calculated temperature and velocity profiles at the exit of a real jet engine show correspondingly even more compact structures of the individual burners in the combustor-turbine intersection.

In future work the turbulent dispersion process of failure structures in the exhaust gas path will be investigated in more detail. This is essential to determine the limit of detectable failure structures behind the aircraft engine. It can already be stated that the turbulent dispersion of inhomogeneous gas phase pattern in the subsequently following turbine is lower than might be anticipated [14], as the large scale turbulent mixing is suppressed from the stator and rotor blades.

These fundamental studies are leading the path to the application of the method of exhaust gas pattern detection to evaluate the internal state of aircraft engines without the need to disassemble the jet engine.

Acknowledgements

This project is funded by the German Research Foundation (DFG) within the framework of the Collaborative Research Centre SFB 871, subproject A4 "Influence of combustion chamber defects on the exhaust jet".

References

1. Adamczuk RR, Buske C, Roehle I, Hennecke C, Dinkelacker F, et al. (2013) Impact of defects and damage in aircraft engines on the exhaust Jet. In: Proceedings of ASME Turbo Expo 2013. ASME, San Antonio, Texas.
2. Vonder-Haar H, Hartmann U, Hennecke C, Dinkelacker F (2016) Defect detection in an annular swirl-burner-array by optical measuring exhaust gases. In: Proceedings of ASME Turbo Expo 2016 ASME.
3. Hennecke C, Frieling D, Dinkelacker F (2013) Influence of combustion chamber disturbances to patterns in the hot gas path. Presented at the European Combustion Meeting 2013, Lund, Schweden.
4. Hennecke C, Maronna T, Dinkelacker F (2013) Detektion von Triebwerks-brennkammerfehlern durch Analyse von Temperatur- und Speziesprofilen der Heißgase einer Modell-Brennkammer. In: VDI-Berichte 2161, Duisburg: 472-480.
5. Menter FR (1994) Two-equation eddy-viscosity turbulence models for engineering applications. *AIAA Journal*. 32 1598-1605.
6. Poinso T, Veynante D (2011) Theoretical and numerical combustion. *Cerfacs*, Toulouse.
7. Jones WP, Whitelaw JH (1982) Calculation methods for reacting turbulent flows: A review. *Combustion and Flame*. 48: 1-26.
8. Gerlinger P (2005) Numerische Verbrennungssimulation: Effiziente numerische Simulation turbulenter Verbrennung. Springer, Berlin.
9. ANSYS (2017) Fluent theory guide.
10. Adrian RJ (1991) Particle-imaging techniques for experimental fluid mechanics. *Ann Rev Fluid Mech* 23: 261-304.
11. Raffel M, Willert CE, Wereley ST, Kompenhans J (2007) Particle image velocimetry: A practical guide with 42 tables. Springer, Berlin.
12. Scheimpflug T (1904) Method of distorting plane images by means of lenses or mirrors. Patents US751347 A.
13. Prasad AK, Jensen K (1995) Scheimpflug stereocamera for particle image velocimetry in liquid flows. *Applied Optics* 34: 7092.
14. Hauptmann T, Aschenbruck J, Christ P, Hennecke C, Dinkelacker F, et al. (2015) Influence of combustion chamber defects on the forced response behavior of turbine blades. Proceedings of the 14th International Symposium on Unsteady Aerodynamics, Aeroacoustics & Aeroelasticity of Turbomachines. 2: 9-19.